

Collimated Energy-Momentum Extraction from Rotating Black Holes in Quasars and Microquasars Using the Penrose Mechanism

Reva Kay Williams^{*† 1}

^{*}*University of Florida, Gainesville, FL 32611*

[†]*Bennett College, Greensboro, NC 27401*

Abstract. For almost four decades, since the discovery of quasars, mounting observational evidence has accumulated that black holes indeed exist in nature. In this paper, I present a theoretical and numerical (Monte Carlo) fully relativistic 4-D analysis of Penrose scattering processes (Compton and $\gamma\gamma \rightarrow e^-e^+$) in the ergosphere of a super-massive Kerr (rotating) black hole. These model calculations surprisingly reveal that the observed high energies and luminosities of quasars and other active galactic nuclei (AGNs), the collimated jets about the polar axis, and the asymmetrical jets (which can be enhanced by relativistic Doppler beaming effects) all are inherent properties of rotating black holes. From this analysis, it is shown that the Penrose scattered escaping relativistic particles exhibit tightly wound coil-like cone distributions (highly collimated vortical jet distributions) about the polar axis, with helical polar angles of escape varying from 0.5° to 30° for the highest energy particles. It is also shown that the gravitomagnetic (GM) field, which causes the dragging of inertial frames, exerts a force acting on the momentum vectors of the incident and scattered particles, causing the particle emission to be asymmetrical above and below the equatorial plane, thus appearing to break the equatorial reflection symmetry of the Kerr metric. When the accretion disk is assumed to be a two-temperature bistable thin disk/ion corona (or torus \equiv advection-dominated accretion flow), energies as high as 54 GeV can be attained by these Penrose processes alone; and when relativistic beaming is included, energies in the TeV range can be achieved, agreeing with observations of some BL Lac objects. When this model is applied specifically to quasars 3C 279 and 3C 273, their observed high energy luminosity spectra can be duplicated and explained. Moreover, this energy extraction model can be applied to any size black hole, irrespective of the mass, and therefore applies to microquasars as well. When applied specifically to microquasar GRS 1915+105 the results are consistent with observations.

¹⁾ E-mail: revak@astro.ufl.edu

I INTRODUCTION

Astrophysical jets are one of the most poorly understood phenomena today. It is clear that they are present where gravitational accretion or contraction and magnetic fields exist. We observe these jets in quasars and microquasars due to supermassive and stellar size black holes, respectively. They are also present in contracting protostars. Perhaps, understanding the mechanism responsible for jets appearing from the energy source of black holes, where the gravitational field is dominant, we can understand their appearances associated with protostars. At present there are two popular trains of thought associated with jets in black holes: one is that the jets are inherent properties of geodesic trajectories in the Kerr [1] metric of a rotating black hole, and thus, can be described by Einstein's general theory of relativity; and the other is that the accretion disk and its magnetic field through magnetohydrodynamics (MHD) are producing the jets. Perhaps it could be a combination of the two, with gravity controlling the flow near the event horizon, and MHD controlling the flow at distances farther away. In this paper, an analysis of the Penrose mechanism [2] is presented to describe gravitational-particle interactions close to the event horizon in the subparsec regime. In this fully general relativistic description, the jets are produced and controlled by gravity alone, without the necessity of an external magnetic field.

II MODEL

The model consists of a supermassive $10^8 M_\odot$ Kerr (rotating) black hole plus particles from an assumed relativistic bistable thin disk/ion corona [or torus \equiv advection-dominated accretion flow (ADAF)]: two-temperature [separate temperatures for protons ($\sim 10^{12}$ K) and electrons ($\sim 10^9$ K)] accretion flow. The Penrose mechanism is used to extract rotational energy-momentum by scattering processes inside the ergosphere ($r_{\text{erg}} \simeq 2M$, where $c = G = 1$). See Williams [3] for a detailed description of the model. The “quasi-Penrose” processes investigated are (a) Penrose Compton scattering (PCS) of equatorial low energy radially infalling photons by equatorially confined ($Q_e = 0$) and nonequatorially confined ($Q_e \neq 0$) orbiting target electrons, at radii between the marginally bound ($r_{\text{mb}} \simeq 1.089M$) and marginally stable ($r_{\text{ms}} \simeq 1.2M$) orbits; (b) Penrose pair production (PPP) ($\gamma p \longrightarrow e^- e^+ p$) at r_{mb} ; (c) PPP ($\gamma \gamma \longrightarrow e^- e^+$) by equatorial low energy radially infalling photons and high energy blueshifted (by factor $\simeq 52$) nonequatorially confined γ -rays at the *photon orbit* ($r_{\text{ph}} \simeq 1.074M$). Note, the target particles are initially in bound (marginally stable or unstable) trapped orbits, trapped in the sense of possibly having no other way of escaping save these Penrose processes [4,3]. Note also that, as the nonequatorially confined target particle passes through the

equatorial plane, Q , a constant of motion as measured by an observer at infinity [5,3], equals P_Θ^2 , where P_Θ is the polar coordinate momentum of the particle.

III METHOD

Monte Carlo computer simulations of up to $\sim 50,000$ scattering events of infalling accretion disk photons (normalized to a power-law distribution) are executed for each quasar. Energy and momentum (i.e., 4-momentum) spectra of escaping particles (γ 's, e^-e^+ 's), as measured by an observer at infinity, are obtained (where $\gamma \equiv$ a general photon, i.e., of any energy value). The following ingredients are used: (1) General relativity [the Kerr metric spacetime geometry yields equatorially and nonequatorially confined ("spherical-like" [6]) particle orbits and escape conditions, conserved energy and angular momentum parameters, and transformations from the Boyer-Lindquist coordinate frame (BLF) to the local nonrotating frame (LNRF)]. Note, BLF is the observer at infinity [7]; LNRF is the local Minkowski (flat) spacetime. (2) Special relativity [in the LNRF, physical processes (i.e., the scatterings) are done; Lorentz transformations between inertial frames are performed; and Lorentz invariant laws are applied]. (3) Cross sections [application of the Monte Carlo method to the cross sections, in the electron rest frame for PCS, in the proton rest frame for PPP($\gamma p \rightarrow e^-e^+p$), and in the center of momentum frame for PPP($\gamma\gamma \rightarrow e^-e^+$), give the distributions of scattering angles and final energies].

IV OVERALL RESULTS

The energies attained are the following: (1) *PCS*: For the input (photon) energy range 5 eV to 1 MeV, the corresponding output energy range is ~ 15 keV to 14 MeV. (2) *PPP* ($\gamma p \rightarrow e^-e^+p$): No escaping pairs for radially infalling γ -rays (~ 40 MeV), and no energy boost: implying that the assumption (negligible recoil energy given to the proton) made in the conventional cross section and, perhaps, the geometry of the scattering must be modified. It had been predicted [8] that pairs with energies (~ 1 GeV) can escape. (3) *PPP* ($\gamma\gamma \rightarrow e^-e^+$): For input (photon) energy range ~ 3.5 keV to 100 MeV, yields output (e^-e^+) energy range ~ 2 MeV to 10 GeV (for BB), and higher up to ~ 54 GeV (for PL, input $\gamma \sim 2$ GeV), where BB, PL \equiv blackbody and power-law distributions, respectively, for the accretion disk protons that yield the neutral pion decays $\pi^0 \rightarrow \gamma\gamma$ [9,10] to populate the photon orbit.

The luminosity spectrum due to Penrose processes for the specific case of quasar 3C 273 is plotted in Figure 1(a), along with the observed spectrum for comparison. The outgoing (escaping) luminosity spectrum produced by the Penrose scattered particles is given by [11]

$$L_\nu^{\text{esc}} \approx 4\pi d^2 F_\nu^{\text{esc}} \quad (\text{erg/s Hz})$$

$$\approx 4\pi d^2 h\nu^{\text{esc}} f_1 f_2 \cdots f_n (N_\nu^{\text{in}} - N_\nu^{\text{cap}}),$$

where d is the cosmological distance of the black hole source; F_ν^{esc} is the flux of escaping photons; N_ν^{in} and N_ν^{cap} are the emittance of incoming and captured photons, respectively; f_n defines the total fraction of the particles that undergoes scattering [$n = 2$ for PCS and $n = 5$ for PPP ($\gamma\gamma \rightarrow e^-e^+$)]. The values of f_1, \dots, f_n are the fitting factors, which make the Penrose calculated luminosities agree with observations for the specific case of 3C 273. Note, in the model calculations, if we let every particle scatter, and set $f_1 = f_3 \sim 10^{-2}$, defining the fraction of the disk luminosity intersecting the scattering regime, with the remaining f_n 's equal 1, the continuum emissions (the top curves on Figures 1(a), labeled with numbers for specific cases of target and incident particles) are obtained; see [11] for details. The spectrum resulting from the PPP ($\gamma\gamma \rightarrow e^-e^+$) is produced by letting the escaping pairs undergo “secondary Penrose Compton scattering” with low energy radially infalling accretion disk photons ($\equiv f_3$).

Thus, as one can see from Figure 1(a), the Penrose mechanism can generate the necessary luminosity observed, and the three model calculated regions of emission [due to PCS by equatorial confined targets (curve passing through nos. 1 – 7), by nonequatorially confined targets that cross the equatorial plane (curve passing through nos. 8 – 13), and PPP ($\gamma\gamma \rightarrow e^-e^+$) (curve passing nos. 14 – 25)] are consistent with the three major regions of emission in all quasars and AGNs. Note, the target photons at the photon orbit can only exist in nonequatorially confined orbits [3].

Moreover, the observed spectra of microquasars (or galactic black holes), in general, appear not to have PCS emission by the nonequatorially confined target electrons, as well as the highest energy γ -ray emission due to PPP ($\gamma\gamma \rightarrow e^-e^+$), indicating that these sources may not have an ion corona nor ADAF, which would be need to populate the orbits to generate such emission.

V THE GRAVITOMAGNETIC FIELD

The gravitomagnetic (GM) force field is the gravitational analog of a magnetic field. It is the additional gravitational force that a rotating mass produces on a test particle. The GM force is produced by the gradient of $\vec{\beta}_{\text{GM}} = -\omega \hat{\mathbf{e}}_\Phi$, where ω is the frame dragging velocity and $\vec{\beta}_{\text{GM}}$ is gravitomagnetic potential [12]. Analysis of the equations governing the trajectories of the particles shows that the GM force, which acts proportional to the momentum of a particle, alters the incoming and outgoing momentum parameters of the incident and scattered particles, resulting in asymmetrical distributions, thus, appearing to break the reflection symmetry of the Kerr metric above and below the equatorial plane [3,13,14]. Effects of the GM force acting on the PPP ($\gamma\gamma \rightarrow e^-e^+$) process can be discerned from Figures 1(d), 1(e), and 2. Note, only the distribution for $(P_{\gamma 2})_\Theta > 0$ is shown in Figure 1. When half of the 2000 target photons are allowed to have $(P_{\gamma 2})_\Theta > 0$ and the other half $(P_{\gamma 2})_\Theta <$

0 of equal absolute values, the e^-e^+ “jet/counter-jet” achieve a maximum ratio $\sim 3 : 1$, favoring $(P_{\mp})_{\Theta} > 0$ [13], as seen in Figure 2. Polar coordinate momentum distributions, $(P'_{\text{ph}})_{\Theta}$, for PCS escaping photons are displayed in Figure 3. Notice the effects of the GM force field causing the photon jet/counter-jet to vary from nearly symmetric to asymmetric for the different cases shown. Of these cases the largest ratio achieved is $\sim 5 : 1$ [Fig. 3(c)]. The direct cause of the asymmetry in the polar direction appears to be due to the severe frame dragging in the ergosphere in which the GM field lines are dragged in the direction that the black hole is rotating [13].

VI THE VORTICAL ORBITS PRODUCED

It is found that the Penrose scattered particles escape along vortical trajectories collimated about the polar axis [3,11,16]. These distributions are fluxes of coil-like trajectories of relativistic jet particles escaping concentric the polar axis. The highest energy escaping particles have the largest P_{Φ} values, the near largest P_{Θ} values, and smallest $|P_r|$ values. Note, P_r is negative (inward toward the polar axis) for most of the PCS photons, and positive for the e^-e^+ pairs. The helical angles of escape $(\delta_i)_{\text{esc}} = |90^\circ - \theta|$ of particle type i , for the highest energy scattered particles are $(\delta_{\text{ph}})_{\text{esc}} \simeq 1^\circ - 30^\circ$ for PCS and $(\delta_{\mp})_{\text{esc}} \sim 25^\circ - 0.5^\circ$ for the e^-e^+ pairs. The above characteristics of the escaping particles imply strong collimation about the polar axis, giving rise to relativistic jets with particle velocities up to $\sim c$ [eg. cf. Figs. 1(b), 1(c), 1(f), and 2]. Note, such vortical trajectories and collimation are consistent with the findings of de Felice et al. from spacetime geometrical studies of general particle geodesics in a Kerr metric [18–20].

VII CONCLUSIONS

From this model to extract energy-momentum from a black hole we can conclude the following: PCS is an effective way to boost soft x-rays to hard x-rays and γ -rays up to ~ 14 MeV. PPP ($\gamma\gamma \longrightarrow e^-e^+$) is an effective way to produce relativistic e^-e^+ pairs up to ~ 54 GeV: This is the probable mechanism producing the fluxes of relativistic pairs emerging from cores of AGNs. These Penrose processes can operate for any size rotating black hole, from quasars to microquasars [17]. Overall, the main features of quasars: (a) high energy particles (x-rays, e^-e^+ pairs, γ -rays) coming from the central source; (b) large luminosities; (c) collimated jets; (d) one-sided (or uneven jets), can all be explained by these Penrose processes to extract energy from a black hole.

Moreover, it is shown here that the geodesic treatment of individual particle processes close to the event horizon in the subparsec regime, as governed by the black hole, is sufficient to described the motion of the particles. This finding is consistent with MHD through the statement made by de Felice and Zanotti [20], that the behavior of such individual particles on geometry (or gravity)-induced

collimated trajectories is also that of the bulk of fluid elements in the guiding center approximation. In light of this, MHD should be incorporated into these calculations to describe the flow of the Penrose escaping particles away from the black hole, i.e., to perhaps further collimate and accelerate these jet particles out to the observed kpc distances.

ACKNOWLEDGMENTS

I first thank God for His thoughts and for making this research possible. Next, I thank Dr. Fernando de Felice and Dr. Henry Kandrup for their helpful comments and discussions. Also, I thank Dr. Roger Penrose for his continual encouragement. I am grateful to the late Dr. Robert (Bob) Hjellming for his helpful discussions and cherished collaboration. Part of this work was done at the Aspen Center for Physics. This work was supported in part by the National Science Foundation and Bennett College.

REFERENCES

1. Kerr, R. P., *Phys. Rev. Letters* **11**, 237 (1963).
2. Penrose, R., *Rivista Del Nuovo Cimento: Numero Speciale* **1**, 252 (1969).
3. Williams, R. K., *Phys Rev. D* **51**, 5387 (1995).
4. Bardeen, J. M., Press, W. H., and Teukolsky, S. A., *Astrophys. J.* **178**, 347 (1972).
5. Carter, B., *Phys Rev.* **174**, 1559 (1968).
6. Wilkins, D. C., *Phys Rev. D* **5**, 814 (1972).
7. Boyer, R. H. and Lindquist, R. W., *J. Math. Phys.* **8**, 265 (1967).
8. Leiter, D. and Kafatos, M., *Astrophys. J.* **226**, 32 (1978).
9. Eilek, J. A., *Astrophys. J* **236**, 664 (1980).
10. Mahadevan, R., Narayan, R., and Krolik, J., *Astrophys. J.* **486**, 268 (1997).
11. Williams, R. K., submitted to *Astrophys. J.*, to appear on this database.
12. K. S. Thorne, R. H. Price, and D. A. Macdonald, *Black Holes: The Membrane Paradigm* (Yale University Press, New Haven, 1986).
13. Williams, R. K., submitted to *Phys. Rev. D*, to appear on this database.
14. Williams, R. K., in *The Proceedings of The Eighth Marcel Grossmann Meeting on General Relativity*, ed. T. Piran & R. Ruffini (Singapore: World Science), 416 (1999).
15. de Felice, F. and Carlotto, L., *Astrophys. J.* **481**, 116 (1997).
16. Williams, R. K., preprint (2000).
17. Williams, R. K. and Hjellming, R. M. (posthumous), to be submitted *Astrophys. J.*, in preparation.
18. de Felice, F. and Curir, A., *Class. Quantum Grav.* **9**, 1303 (1992).
19. de Felice, F. and Carlotto, L., *Astrophys. J.* **481**, 116 (1997).
20. de Felice, F. and Zanotti, O., *Gen. Rel. Grav.* **8**, No. 32, 1449 (2000).

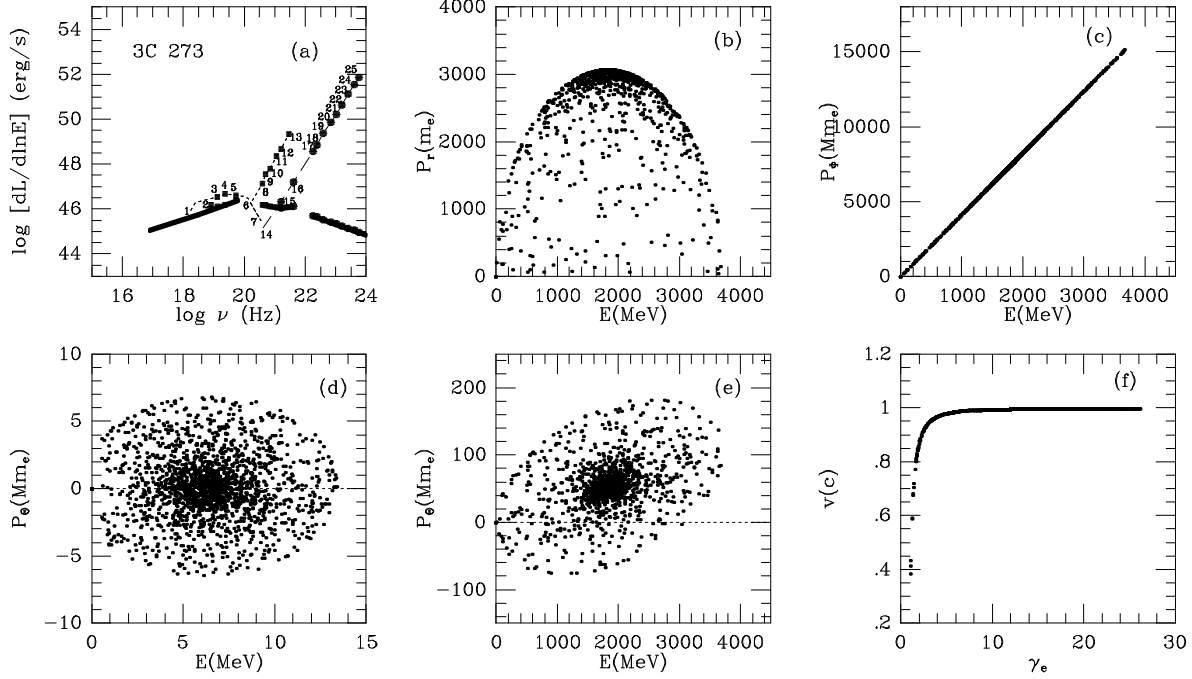


FIGURE 1. (a) Comparing the theoretical spectrum with observations for 3C 273. The calculated PCS and PPP ($\gamma\gamma \rightarrow e^-e^+$) luminosity spectra are represented by the solid squares and large solid dots, respectively. The observed spectra is indicated by the solid line. The upper curves with the solid squares and solid dots superimposed on the dotted line and the dashed line, respectively, for PCS and PPP ($\gamma\gamma \rightarrow e^-e^+$), are the spectra calculated from this model. Superimposed on the lower solid line of the observations are solid squares and solid dots that have been adjusted to agree with observations. These adjustments depend on the f_n 's values (see text). (b) and (c) PPP ($\gamma\gamma \rightarrow e^-e^+$) at $r_{ph} = 1.074M$: scatter plots showing momentum components (each point represents a scattering event). The radial momenta $(P_\mp)_r$ vs. E_\mp , the azimuthal momenta $(P_\mp)_\phi$ ($\equiv L_\mp$) vs. E_\mp ; for the infalling photons $E_{\gamma 1} = 0.03$ MeV, and for the target photons $E_{\gamma 2} = 3.893$ GeV. (d) and (e) PPP ($\gamma\gamma \rightarrow e^-e^+$): $(P_\mp)_\theta$ vs. E_\mp ; for $E_{\gamma 1} = 0.03$ MeV, $E_{\gamma 2} = 13.54$ MeV, $(P_{\gamma 2})_\theta = 0.393 Mm_e$; and for $E_{\gamma 1} = 0.03$ MeV, $E_{\gamma 2} = 3.893$ GeV, $(P_{\gamma 2})_\theta = 113 Mm_e$; respectively. (f) The velocity distribution vs. $\gamma_e (= E_\mp/m_e c^2)$ for the same case as (d) above.

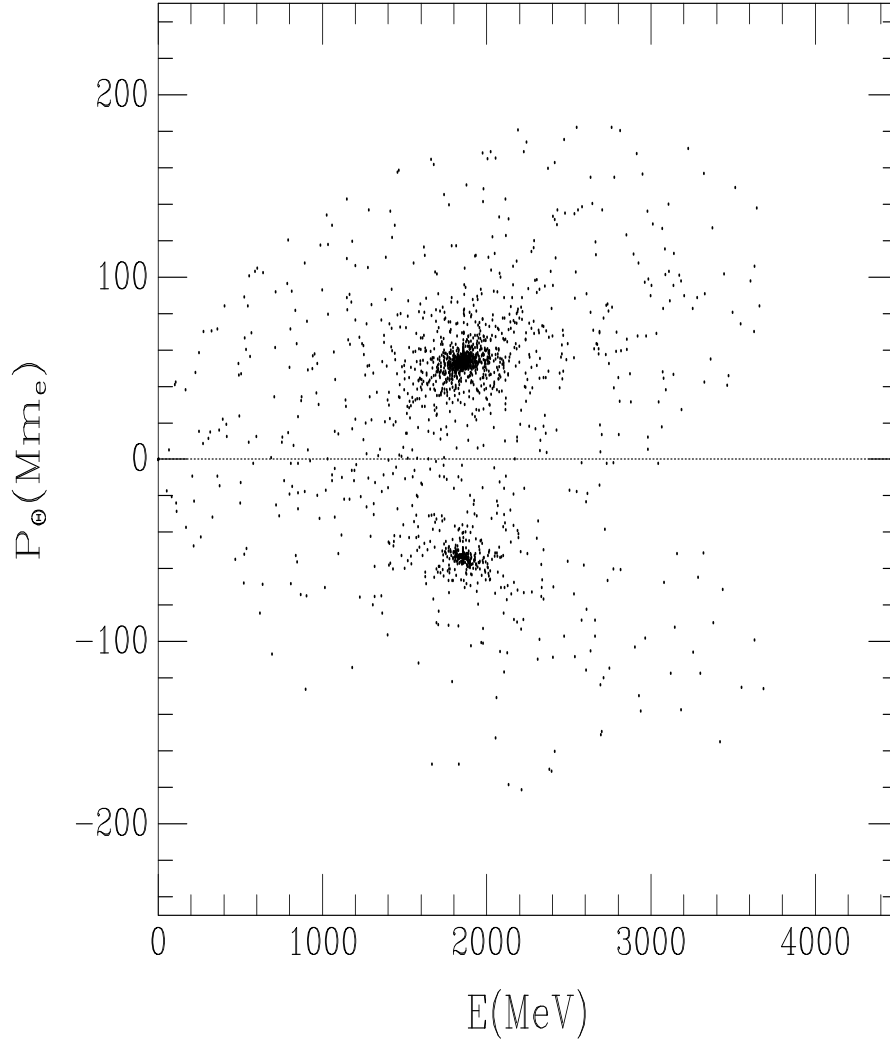


FIGURE 2. PPP ($\gamma\gamma \longrightarrow e^-e^+$) at $r_{\text{ph}} = 1.074M$: scatter plots showing momentum components (each point represents a scattering event); for the infalling photons $E_{\gamma 1} = 0.03$ MeV, and for the target photons $E_{\gamma 2} = 3.893$ GeV, $(P_{\gamma 2})_\Theta = \pm 113 Mm_e$ [similar to Fig. 1(e); see text].

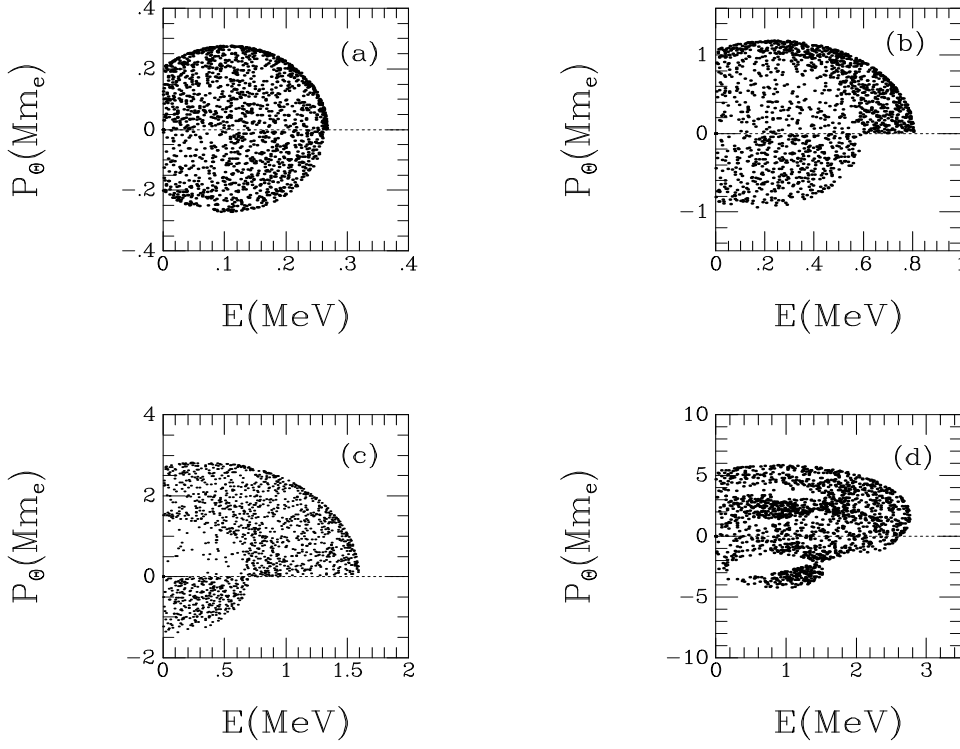


FIGURE 3. PCS: scatter plots showing polar coordinate space momenta: $(P'_{\text{ph}})_{\Theta} [\equiv (Q'_{\text{ph}})^{1/2}]$ vs. E'_{ph} , of the escaping PCS photons after 2000 events (each point represents a scattering event), at $r_{\text{mb}} \simeq 1.089M$. The various cases are defined by the following parameters: E_{ph} , initial photon energy; E_e , the target electron orbital energy; $Q_e^{1/2}$, defining the corresponding polar coordinate momentum $(P_e)_{\Theta}$ of the target electron; N_{es} , number of photons escaping. (a) $E_{\text{ph}} = 3.5$ keV, $E_e = 0.539$ MeV, $Q_e^{1/2} = 0$, $N_{\text{es}} = 1637$. (b) $E_{\text{ph}} = 0.03$ MeV, $E_e = 0.539$ MeV, $Q_e^{1/2} = 0$, $N_{\text{es}} = 1521$. (c) $E_{\text{ph}} = 0.15$ MeV, $Q_e^{1/2} = 0$, $N_{\text{es}} = 1442$. (d) $E_{\text{ph}} = 0.15$ MeV, $E_e = 1.297$ MeV, $Q_e^{1/2} = \pm 2.479 Mm_e$, $N_{\text{es}} = 1628$. (Note, due to a minor oversight leading to improper treatment in the computer simulation of the arccosine term in eq. (3.39) of [3], correct Figs. 3(a) and 3(b) presented here replace Figs. 7(a) and 3(c), respectively, of [3].)